


RESEARCH ARTICLE OPEN ACCESS

Assessment of Vertebral Bone Marrow Perfusion, Fat/Water Content, and Trabecular Bone Changes Using Multimodal MRI and Micro-CT in a Rat Model of Chronic Kidney Disease

Guo-Shu Huang^{1,2} | Shih-Wei Chiang¹ | Yi-Jen Peng³ | Skye Hsin-Hsien Yeh⁴ | Yu-Juei Hsu⁵ | Yu-Ching Chou⁶ | Heng-Han Chang⁷ | Heng-Sheng Lee^{3,8} | Ying-Chun Liu^{1,7} | Chao-Ying Wang^{7,9} 

¹Department of Radiology, Tri-Service General Hospital, National Defense Medical Center, Taipei, Taiwan | ²Department of Medical Research, Tri-Service General Hospital, National Defense Medical Center, Taipei, Taiwan | ³Department of Pathology, Tri-Service General Hospital, National Defense Medical Center, Taipei, Taiwan | ⁴Brain Research Center, School of Medicine, National Defense Medical Center, Taipei, Taiwan | ⁵Division of Nephrology, Department of Medicine, Tri-Service General Hospital, National Defense Medical Center, Taipei, Taiwan | ⁶School of Public Health, National Defense Medical Center, Taipei, Taiwan | ⁷Department and Graduate Institute of Biology and Anatomy, National Defense Medical Center, Taipei, Taiwan | ⁸Department of Pathology and Laboratory Medicine, Kaohsiung Veterans General Hospital, Kaohsiung, Taiwan | ⁹Instrument Center, National Defense Medical Center, Taipei, Taiwan

Correspondence: Chao-Ying Wang (charliewcy@gmail.com)

Received: 20 September 2024 | **Revised:** 4 December 2024 | **Accepted:** 31 December 2024

Funding: This work was supported by the National Science and Technology Council (MOST102-2628-B-016-004-MY3 and MOST108-2314-B-016-007-MY2) and the Civilian Foundation of Tri-Service General Hospital (TSGH-C103-051 and TSGH-C104-048).

Keywords: CKD | DCE-MRI | MRS | perfusion | T2* quantification | vertebral bone marrow | μ CT

ABSTRACT

Background: Disturbances in calcium and phosphorus homeostasis resulting from chronic kidney disease (CKD) may lead to atherosclerotic changes in blood vessels, potentially altering bone marrow perfusion. Our study aimed to investigate vertebral bone marrow perfusion using dynamic contrast-enhanced (DCE) MRI with a pharmacokinetic model. We also measured possible changes in water and fat content and bony trabeculae using T2* quantification, MR spectroscopy (MRS), and microcomputed tomography (μ CT).

Methods: Twelve rats were randomly separated into a normal control group and a CKD (5/6 nephrectomy) group. Their lumbar spines were imaged, with monitoring of the L5 vertebral body conducted at 0, 8, 16, 30, and 43 weeks. After Week 43, all rats were sacrificed, and histologic changes were correlated with MRI and μ CT results.

Results: The CKD group demonstrated significantly lower A and k_{el} values ($p < 0.05$), significantly increased T2* values ($p < 0.05$), significantly decreased fat content and trabeculation ($p < 0.05$), sinusoidal dilatation, and decreased adipocytes in the vertebral bone marrow.

Conclusion: Using quantitative MRI and μ CT to assess CKD-related arthropathy of the vertebral body is feasible. Lumbar spine bone marrow perfusion deficiency in experimental CKD may be associated with decreased fat content, increased water content, and sparse trabeculation.

The first two authors contributed equally to this article.

This is an open access article under the terms of the [Creative Commons Attribution-NonCommercial-NoDerivs](https://creativecommons.org/licenses/by-nc-nd/4.0/) License, which permits use and distribution in any medium, provided the original work is properly cited, the use is non-commercial and no modifications or adaptations are made.

© 2025 The Author(s). JOR Spine published by Wiley Periodicals LLC on behalf of Orthopaedic Research Society.

1 | Introduction

Chronic kidney disease (CKD) is a progressive condition characterized by structural and functional abnormalities in the kidneys, ultimately leading to kidney damage and failure. Evidence indicates that CKD patients who develop cardiovascular diseases have a 1.5- to 3-fold higher mortality rate compared to the general CKD population, underscoring cardiovascular disease as a major risk factor for mortality in CKD [1–3]. Impaired renal function in CKD causes hyperphosphatemia, triggering a cascade of events involving increased release of fibroblast growth factor (FGF)–23 from bones, reduced intestinal calcium absorption, elevated PTH levels, calcium efflux from bones, and subsequent vascular calcification. The pathological interplay among the kidneys, bones, and vasculature, termed the kidney–bone–vascular axis, perpetuates dysregulated mineral metabolism and potentiates the development of systemic complications in CKD [4–6]. This leads to calcium phosphate deposition in blood vessels, causing thickening and vascular calcification, which may worsen bone damage [7–9]. The vertebral bones serve crucial structural and functional roles in the human body, providing weight-bearing support, facilitating movement, and safeguarding the spinal cord. Notably, the lower lumbar region, encompassing the fifth lumbar vertebra (L5) and the first sacral vertebra (S1), is a common site of low back pain and various spinal pathologies [10, 11]. Furthermore, the vertebral bones serve as vital hematopoietic organs, with the vertebral bodies housing hematopoietic red bone marrow, a rich reservoir of blood cell precursors. These precursor cells play a dynamic role in replenishing the body's cellular requirements and adapting to varying physiological states [12, 13]. However, the hematopoietic cells within the bone marrow undergo a gradual age-related transition to yellow marrow, and certain disease states may also impact this susceptible organ. The present study endeavors to elucidate whether CKD influences these transformative processes and explores the potential role of the associated alterations in blood flow.

Dynamic contrast-enhanced MRI (DCE-MRI) is an advanced imaging technique capable of assessing microvascular permeability changes by combining paramagnetic contrast agents with dynamic imaging. While extensively validated and widely adopted in oncology and vascular disease studies [14–17], DCE-MRI is rarely used in musculoskeletal system studies. DCE-MRI investigations are often limited to qualitative descriptions or semi-quantification of parameters such as time-to-peak, slope, and maximum enhancement [18]. The use of DCE-MRI for quantitative pharmacokinetic modeling and compartmental approaches to simulate the intricate blood flow–tissue relationship and facilitate in-depth analysis of microcirculatory physiology despite limited spatial resolution, is even less frequent. In this study, pharmacokinetic modeling is employed to quantitatively analyze vertebral DCE-MRI data and thereby elucidate the potential impacts of CKD on nutrient delivery to the highly vascularized vertebral bone marrow. T2* quantification involves measuring T2* relaxation times in tissues, enabling observation of physiological characteristics. Unlike conventional methods of T2 quantification without 180 degree refocusing pulses, the T2* method effectively detects tissues with rapid signal decay, such as short-T2 tissues like

articular cartilage. Prior studies have demonstrated strong correlations between T2 values and pathologies, including osteoarthritis-related collagen loss and trauma-induced edema or degeneration in spinal bone marrow [19, 20]. In this study, T2* quantification was favored over T2 quantification due to the limited literature on CKD-induced bone marrow T2 alterations and the extremely short T2 values in adjacent intervertebral discs. CKD-related microcirculatory changes may induce hypoxia, edema, or degeneration in bone marrow regions. Consequently, to provide insights into bone marrow health status, quantitative T2* values were utilized in the present study to assess alterations in bone marrow water content resulting from CKD.

Magnetic resonance spectroscopy (MRS) utilizes electron cloud shielding effects under strong magnetic fields to observe in vivo changes in specific chemical compound concentrations, thereby enabling the study of biochemical processes within biological systems. Beyond brain applications, MRS has provided substantial insights in musculoskeletal studies, demonstrating correlations between intramuscular fat and type 2 diabetes, quantifying subcutaneous fat depletion in HIV patients during antiretroviral therapy, and investigating the osteoporosis-fat content relationship, particularly in postmenopausal cases [21–23]. Accordingly, MRS has emerged as a convenient and accurate tool for quantifying specific chemical compounds in vivo [24]. Consequently, MRS was used here to assess changes in fat composition.

Given the limited research exploring the relationship between blood flow and bone marrow pathologies in CKD, this study aimed to investigate whether advanced MRI techniques, combined with microcomputed tomography (μ CT), can elucidate potential alterations in perfusion, water content, fat composition, and bone structure within the vertebral bone marrow microenvironment during CKD progression. It also sought to correlate these findings to gain insights into underlying pathogenic mechanisms. To investigate CKD's impact on vertebral bone marrow perfusion, this longitudinal study employed a 5/6 nephrectomy animal model. Concurrently, T2* quantification was used to assess potential water content changes resulting from perfusion alterations, while MRS was used to evaluate changes in bone marrow fat composition. Associations between these findings and changes in bone mass were also explored. By utilizing this non-invasive, longitudinal animal imaging approach, we aimed to enhance the understanding of CKD, potentially translating these insights to human studies and contributing to improved disease monitoring and therapeutic strategies.

2 | Materials and Methods

2.1 | Ethical Statement for This Study

The study experiments were performed in accordance with the *Guide for the Care and Use of Laboratory Animals* established by the U.S. National Institutes of Health. All animal experiments conducted in this study were approved by the Institutional Animal Care and Use Committee (IACUC) of the National Defense Medical Center and performed in

accordance with the 3Rs (Replacement, Reduction, and Refinement) principles. The IACUC approval number for this study is IACUC-19-155. Isoflurane anesthesia was used in all animal experiments.

2.2 | Animal Experiments

The experiment utilized 8-week-old male Sprague Dawley rats, weighing approximately 300g. The experimental design consisted of two groups: a control group of six rats and a CKD group of six rats. After a 1-week acclimatization period, the CKD group underwent a two-stage 5/6 nephrectomy procedure to induce CKD [25]. In the first stage, electrocautery was used to destroy 2/3 of the left kidney (one-third of the upper and lower poles). One week later, the second stage involved the complete removal of the right kidney. The control group rats did not undergo any surgical procedure. After the 5/6 nephrectomy in the CKD group, blood and urine samples were collected from both the control and CKD groups 1 day before the MRI scans. These samples were analyzed for biochemical indicators, such as blood urea nitrogen, serum creatinine, and urine protein levels, to confirm the successful induction of CKD. The week after the 5/6 nephrectomy was defined as Week 0 for the CKD group. MRI scans, including DCE-MRI, T2* quantification, and MRS, were conducted at Weeks 0, 8, 16, 30, and 43. After completing the MRI experiments at Week 43, the rats were sacrificed for μ CT and histological staining experiments.

All rats were anesthetized through inhalation of a 5% isoflurane mixture administered at an oxygen flow rate of 5 L/min and then placed into a body holder. A maximum of three rats were housed together in one cage within a specific pathogen-free environment. The animals were kept under a 12-h light/12-h dark cycle at a temperature of $21^{\circ}\text{C} \pm 2^{\circ}\text{C}$ and humidity of $50\% \pm 5\%$. They were fed with 5053-PicoLab Rodent Diet 20. Continuous monitoring of the animals was conducted before, during, and after the experiment. The MRI experiment was conducted using a 4.7T magnet (Bruker, Ettlingen, Germany) equipped with a receiver quadrature surface coil positioned above the lumbar spine. Anesthetic depth was maintained by providing 1%–2% isoflurane at an oxygen flow rate of 2 L/min.

2.3 | DCE-MRI of Lumbar Spine

DCE-MRI was performed using a fast gradient echo (GRE) technique with the following parameters: repetition time (TR): 202 ms, echo time (TE): 3.5 ms, number of excitations (NEX): 1, matrix size: 64×128 reconstructed to 128×128 , field of view (FOV): $40 \times 40 \text{ mm}^2$, slice thickness: 0.7 mm, flip angle = 60° , and total acquisition time of 18 min 46 s. Localization was achieved using T2-weighted fast spin-echo transverse images of the L5 vertebra. Six consecutive sagittal plane DCE-MRI slices were obtained, covering the left to right transverse processes of the lumbar spine. After an intravenous bolus injection of 0.2 mmol/kg gadobutrol contrast agent (Gadovist, Bayer Schering, Berlin, Germany) via the tail vein, a series of 80 continuous dynamic images were acquired starting at 60 s post-injection. A total of 480 dynamic images were obtained, and finally, 0.5 mL of saline was injected to flush any remaining contrast agent from the catheter into the rat.

A total of 480 images (6 slices/set, 80 sets) were acquired during the DCE-MRI scan. After acquisition, the images were transferred to an independent analysis workstation, and L5 vertebral bone perfusion analysis was performed using the MISTar software (Apollo Medical Imaging Technology, North Melbourne, Australia). The analysis module employed was the two-compartmental Brix model [26]. The mean signal intensities within the regions of interest (ROIs) were computed and subsequently converted into concentration-time data. Subsequently, the concentration-time data underwent a fitting process utilizing the Brix pharmacokinetic model, which employed a nonlinear least-square curve fitting algorithm [27, 28]. Three perfusion parameters, amplitude (A), elimination constant (k_{el}), and permeability rate constant (k_{ep}), were estimated from a pixel-wise analysis of the L5 vertebra ROI selected manually, as shown in Figure 1.

2.4 | T2* Quantification of Lumbar Spine

T2* quantification was acquired using a multi-echo gradient echo technique with eight echo times (TEs) of 3.8, 9.6, 15.5, 21.3, 27.1, 33.0, 38.9, and 44.7 ms. Other parameters were as follows: TR = 600 ms, FOV = $40 \times 40 \text{ mm}^2$, NEX = 12, matrix size = 128×128 reconstructed to 256×256 , slice thickness = 0.7 mm, flip angle = 30° , and six sagittal slices were collected with a total scan time of 15 min 22 s. Post-processing analysis of T2* quantitative images was performed using

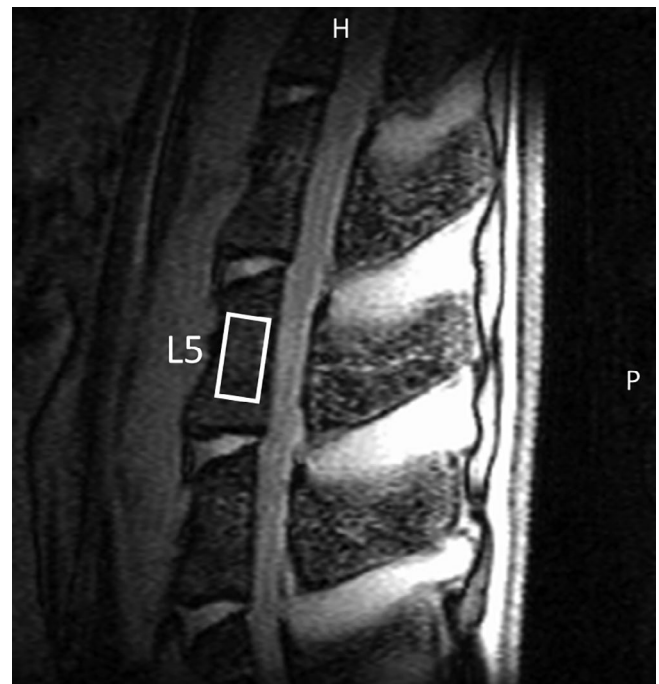


FIGURE 1 | The region of interest (ROI) in the fifth lumbar vertebral bone marrow. A rectangular ROI was located at the fifth lumbar vertebra (L5) in the vertebral body above the second sacral level. The area was drawn manually, excluding the upper and lower borders near the subchondral bone and endplate cartilage. For ROI positioning and parametric analysis, we used the sagittal midline image showing the maximal selectable vertebral body. The letter “H” denotes the head position, while “P” indicates the posterior position.

MR-Vision software (Winchester, MA, USA). The MRI T2* relaxation time of the lumbar spine was analyzed using the single-exponential, least-squares curve-fitting method, which was selected for its ability to minimize fitting errors in images characterized by a low signal-to-noise ratio [29]. The spin density (M_0) and apparent transverse relaxation time (T2*) were determined by fitting the multi-echo decay curve to a mono-exponential decay model. The L5 vertebrae bone marrow was manually segmented from the first-frame T2* quantification images, as shown in Figure 1. To minimize variability in the manual delineation of ROIs, two independent image analysts (C.Y.W. and S.W.C.) performed the ROI delineation. These ROIs were subsequently verified by an experienced musculoskeletal radiologist (G.S.H.). The results presented in this study represent the mean values of the measurements obtained by both analysts.

2.5 | MRS of Lumbar Spine

For the MR spectroscopy scans, the point-resolved spectroscopy sequence (PRESS) was used for sampling. Localization was achieved using three orthogonal gradient-echo (GRE) images, and the volume of interest was positioned at the center of the L5 vertebral bone marrow using the sagittal GRE slice (as illustrated in Figure 1). The PRESS sequence parameters were as follows: TR: 3000 ms, TE: 35 ms, NEX: 512, voxel size: $1 \times 1 \times 1 \text{ mm}^3$, bandwidth: 4960.3 Hz, with no water suppression pulse to retain the water peak for calculation, and scan time: 25 min 36 s. Post-processing of the spectral data was performed using the ParaVision 360 spectral analysis software. All spectra underwent apodization with an 8-Hz Gaussian filter, followed by automatic phase correction, zero-filling, and baseline correction. Spectral interpretation and calculation were then carried out. For fat content, the fat fraction (FF) of vertebral bone marrow, representing the relative fat content, was calculated as the ratio of the integral of the fat peak at 1.33 ppm to the sum of the integrals of the water peak at 4.7 ppm and the fat peak [30, 31].

2.6 | Microcomputed Tomography of Lumbar Spine

After completion of the final MRI at Week 43, the animals were euthanized, and their lumbar vertebrae were extracted for subsequent μ CT assessment. Micro-CT was performed on the ex vivo lumbar vertebrae of rats using a 360° cone-beam acquisition on a SkyScan 1076 scanner (Bruker, Kontich, Belgium). The parameters of X-ray source were set to 59 kVp and 167 μ A, voxel size = 18 μm^3 , exposure time = 500 ms per frame, with images acquired at 0.8° increments over a total of 360°. The total scan time was 7 min 16 s. After μ CT scanning, post-processing and analysis were carried out using the manufacturer's reconstruction software CTAn 32 and CTVol 32. The region of interest was manually selected on the mid-transverse slice at the L5 vertebral body, excluding the cortical bone and isolating the trabecular bone compartment [32, 33]. The images of the L5 lumbar vertebra were reconstructed from 2D data and presented as a 3D volume rendering. Four trabecular parameters were quantified: bone volume fraction (bone volume/total volume, BV/TV, unit: %), trabecular thickness (Tb.Th, unit: μm), trabecular number (Tb.N, unit: mm^{-1}), and trabecular separation (Tb.Sp, unit: μm).

2.7 | Histologic Analysis

The abdominal aorta and lumbar vertebrae were harvested, sectioned, and stained with hematoxylin and eosin (H&E). Samples were fixed in 10% neutral buffered formalin for approximately 12 h. Lumbar vertebrae underwent decalcification using a rapid decalcifier solution (Nihon Shiyaku Industries, Osaka, Japan) for 24 h. Following decalcification, samples were thoroughly washed with running water to remove residual acid and prevent interference with subsequent processing steps. After dehydration, samples were embedded in paraffin. Due to the minimal diameters of the lumbar segmental medullary arteries in rats, surgical retrieval is rendered impractical. Therefore, the histological analysis of vessels focused on the abdominal aorta—the source of lumbar blood flow—to assess the vascular wall thickness and calcification. Sections were cut at 5 μm thickness and examined under a microscope at 400x magnification. Images were acquired using Aperio ImageScope version 12. Vascular structures and vertebral bone marrow samples from both experimental groups were analyzed to validate the observations obtained through MRI and μ CT analyses. A comprehensive histological analysis was performed by quantifying three parameters: vascular density (vessels/ mm^2), adipose tissue composition (lipid area percentage), and trabecular bone proportion (trabecular area percentage).

2.8 | Statistical Analysis

The mean and 95% confidence interval (CI) were calculated for DCE-MRI, T2*, MRS, μ CT, and histology parameters in both the control and CKD groups. To account for within-subject correlations arising from repeated measurements, generalized estimating equations (GEEs) were employed for multiple linear regression analyses [34]. The models included main effects for group (control vs. CKD), time point (0, 8, 16, 30, and 43 weeks), and their interaction term to assess between-group differences in the longitudinal trajectories of MRI measures relative to baseline [35]. The reproducibility of DCE-MRI, T2*, and FF values was evaluated using the intraclass correlation coefficient (ICC). Reliability was assessed using a two-way mixed-effects model (ICC3, 1) with absolute agreement. The first ICC number 3 refers to the two-way mixed effects model (Model 3), and the second ICC number 1 refers to the type of ICC calculation with single rater/measurement. ICC values approaching 1 indicate higher reproducibility, with values greater than 0.75 generally considered excellent [36, 37]. All statistical analyses were conducted using SPSS version 26.0 software (SPSS Inc., Chicago, IL, USA), with p -values < 0.05 considered statistically significant.

3 | Results

No adverse events were noted. The successful induction of CKD following 5/6 nephrectomy was confirmed through biochemical analysis. For all rats, the interobserver correlation coefficients were high (DCE: $r = 0.905$, T2*: $r = 0.957$, and FF: $r = 0.985$). The intra-observer correlation coefficient of the DCE-MRI, T2*, and FF values was 0.936, 0.905, and 0.974, respectively, indicating good reproducibility.

3.1 | DCE-MRI Analysis

GEE multiple linear regression analysis was performed. At baseline (Week 0), no significant differences were observed between groups for the three perfusion parameters A , k_{el} , and k_{ep} ($p=0.229-0.681$). In the control group, perfusion parameters (A and k_{ep}) at 43 weeks were statistically significantly decreased compared with their baseline values (p -values 0.04, <0.001, respectively). No significant difference was found in the perfusion

parameter k_{el} across different time points. Compared to the control group, the CKD group exhibited significantly lower perfusion parameters A at 30 and 43 weeks (p -values 0.047–0.002, Table 1 and Figure 2A), and k_{el} at 16, 30, and 43 weeks (p -values 0.003 to <0.001, Table 2 and Figure 2B). No significant difference was found in the perfusion parameter k_{ep} across different time points between the control and CKD groups (Table 3, Figure 2C). Representative A and k_{el} images are shown in Figure 3A,B. Our findings indicate that DCE-MRI analysis is

TABLE 1 | Longitudinal comparison of the perfusion parameter A between the control and CKD groups using GEE analysis over a 43-week period.

	Parameters	B	Std. error	95% Wald CI		p
Parameter A	Intercept	1.005	0.0479	0.911	1.099	<0.001
	CKD vs. control	0.027	0.0649	-0.101	0.154	0.681
Evaluate temporal deviations from Week 0 in the control group	[Week = 43] vs. [Week = 0]	-0.167	0.0582	-0.281	-0.053	0.004
	[Week = 30] vs. [Week = 0]	-0.098	0.0664	-0.228	0.032	0.139
	[Week = 16] vs. [Week = 0]	-0.073	0.0469	-0.165	0.019	0.118
	[Week = 8] vs. [Week = 0]	-0.047	0.0330	-0.111	0.018	0.157
Evaluate intergroup differences in temporal variations between the CKD and control groups	[Week = 43]	-0.215	0.0680	-0.348	-0.082	0.002
	[Week = 30]	-0.178	0.0898	-0.354	-0.002	0.047
	[Week = 16]	-0.148	0.1017	-0.348	0.051	0.145
	[Week = 8]	-0.072	0.0569	-0.183	0.040	0.208

Note: B : regression coefficient, * p value < 0.05.

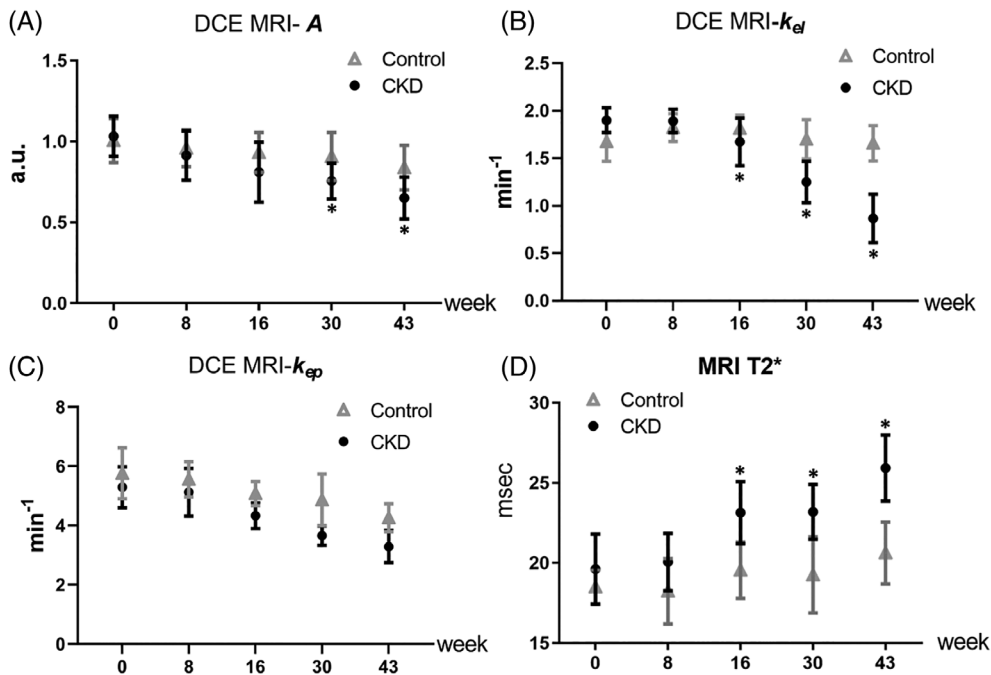


FIGURE 2 | Sequential changes in DCE-MRI and T2 values at different weeks. The perfusion parameters A (a.u.), k_{el} (unit: Min^{-1}), and k_{ep} (unit: Min^{-1}), as well as the $T2^*$ value (msec), were quantified for all subjects at Weeks 0, 8, 16, 30, and 43. Statistical significance ($p < 0.05$) is indicated by asterisks. Open triangles indicate the control group, while filled circles represent the CKD group. (A) Significantly decreasing changes in DCE-MRI parameter A were observed in the CKD group compared to the control group from Week 30 onward. (B) Regarding the wash-out parameter k_{el} , decreasing values were observed at Weeks 16, 30, and 43. (C) No significant findings were observed in the permeability parameter k_{ep} from 0 to 43 weeks. (D) $T2^*$ values were significantly higher from Week 16 to 43 in the CKD group.

TABLE 2 | Longitudinal comparison of perfusion parameter k_{el} between the control and CKD groups using GEE analysis over a 43-week period.

	Parameters	B	Std. error	95% Wald CI		p
Parameter k_{el}	Intercept	1.675	0.0737	1.531	1.819	< 0.001
	CKD vs. control	0.227	0.0871	0.056	0.397	0.309
Evaluate temporal deviations from Week 0 in the control group	[Week = 43] vs. [Week = 0]	-0.017	0.1238	-0.259	0.226	0.893
	[Week = 30] vs. [Week = 0]	0.027	0.0914	-0.153	0.206	0.771
	[Week = 16] vs. [Week = 0]	0.140	0.0782	-0.013	0.293	0.074
	[Week = 8] vs. [Week = 0]	0.148	0.0735	0.004	0.292	0.443
Evaluate intergroup differences in temporal variations between the CKD and control groups	[Week = 43]	-1.018	0.1656	-1.343	-0.694	< 0.001
	[Week = 30]	-0.678	0.1444	-0.961	-0.395	< 0.001
	[Week = 16]	-0.368	0.1230	-0.609	-0.127	0.003
	[Week = 8]	-0.157	0.0847	-0.323	0.009	0.064

Note: B: regression coefficient, *p value < 0.05.

TABLE 3 | Longitudinal comparison of perfusion parameter k_{ep} between the control and CKD groups using GEE analysis over a 43-week period.

	Parameters	B	Std. error	95% Wald CI		p
Parameter k_{ep}	Intercept	5.758	0.3039	5.163	6.354	< 0.001
	CKD vs. control	-0.470	0.3904	-1.235	0.295	0.229
Evaluate temporal deviations from Week 0 in the control group	[Week = 43] vs. [Week = 0]	-1.502	0.4099	-2.305	-0.698	< 0.001
	[Week = 30] vs. [Week = 0]	-0.892	0.5089	-1.889	0.106	0.080
	[Week = 16] vs. [Week = 0]	-0.682	0.3513	-1.370	0.007	0.052
	[Week = 8] vs. [Week = 0]	-0.203	0.1649	-0.527	0.120	0.218
Evaluate intergroup differences in temporal variations between the CKD and control groups	[Week = 43]	-0.502	0.4605	-1.404	0.401	0.276
	[Week = 30]	-0.742	0.5352	-1.791	0.307	0.166
	[Week = 16]	-0.280	0.3849	-1.034	0.474	0.467
	[Week = 8]	0.035	0.1943	-0.346	0.416	0.857

Note: B: regression coefficient, *p value < 0.05.

capable of detecting the reduction in vertebral bone marrow perfusion associated with CKD progression.

3.2 | MRI T2* Analysis

In T2* analysis, no significant between-group difference at Week 0 was shown in multiple linear regression using the GEE method (p -value = 0.20). In the control group, no significant difference in T2* values was observed from Weeks 8 to 30 (p -values = 0.097–0.724) compared to baseline. However, a mild increase in T2* values was noted at 43 weeks relative to baseline (p -value = 0.001). When comparing the T2* values of the CKD to those of the control group, mildly but not significantly increased values were found in the CKD group at Week 8 (p -value = 0.39). From Weeks 16 to 43, the CKD group exhibited significantly higher T2* values than controls, with p -values ranging from 0.023 to < 0.001 (Table 4, Figure 2D). Higher signal intensity is evident in the T2* quantification maps presented in Figure 3C, signifying the development of bone marrow edema.

3.3 | MRS Analysis

Single-voxel proton (^1H) MRS was employed to quantify alterations in vertebral bone marrow fat content at the L5 level of all rats. At Week 0, no significant between-group difference was shown (p -value = 0.679, Figure 4A). In the control group, results demonstrated a significant increase in FF ratio values over the course of the study compared to baseline from Weeks 8, 16, and 30 to 43 (all p -values < 0.001). Similarly, a significant increase in FF ratio values was found in the CKD group from Weeks 8 to 43 compared to baseline. However, relative to controls, the CKD group exhibited comparatively lower vertebral bone marrow fat fractions. At Week 8, no statistically significant difference in FF was detected between the two groups (p -value = 0.317). From Weeks 16 to 43, the CKD group manifested significantly decreased fat fractions when compared to controls (all p -values < 0.001, Figure 4B), as illustrated in Table 5. Representative MR spectra depicting these findings are provided in Figure 4A. The results suggest that MRS analysis can be used to detect the decline in vertebral bone marrow fat content as CKD progresses.

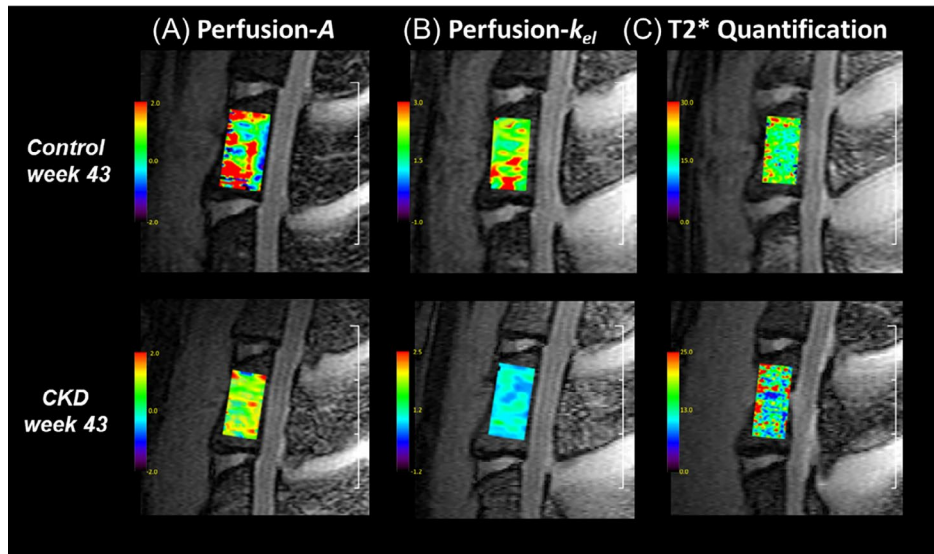


FIGURE 3 | Perfusion parameter A , k_{el} , and $T2^*$ quantification maps of vertebral bone marrow between groups. (A) DCE-MRI A maps of the vertebral bone marrow at Week 43 post-intervention. Color-coded images demonstrate markedly lower signal intensity in CKD rats (bottom) relative to controls (top), indicating blood flow deficiency in the bone marrow regions. (B) Wash-out k_{el} maps show significant signal loss in CKD rats compared to controls, indicating delayed blood flow wash-out. (C) $T2^*$ quantification maps reveal significantly elevated $T2^*$ values in CKD rats (bottom) compared to controls (top).

TABLE 4 | Longitudinal comparison of $T2^*$ values between the control and CKD groups using GEE analysis over a 43-week period.

	Parameters	B	Std. error	95% Wald CI		p
T2* values	Intercept	18.508	0.3706	17.782	19.235	< 0.001
	CKD vs. control	1.105	0.8624	-0.585	2.795	0.200
Evaluate temporal deviations from Week 0 in the control group	[Week = 43] vs. [Week = 0]	2.122	0.6454	0.857	3.387	0.001
	[Week = 30] vs. [Week = 0]	0.753	0.9219	-1.054	2.560	0.414
	[Week = 16] vs. [Week = 0]	1.043	0.6286	-0.189	2.275	0.097
	[Week = 8] vs. [Week = 0]	-0.270	0.7639	-1.767	1.227	0.724
Evaluate intergroup differences in temporal variations between the CKD and control groups	[Week = 43]	4.195	1.0084	2.219	6.171	< 0.001
	[Week = 30]	2.828	1.2400	0.398	5.259	0.023
	[Week = 16]	2.488	0.7822	0.955	4.021	0.001
	[Week = 8]	0.722	0.8397	-0.924	2.367	0.390

Note: B : regression coefficient, * p value < 0.05.

3.4 | Micro-CT Analysis

Consistent with the MRI protocol, the micro-CT analysis was centered on the L5 vertebral body by delineating the same ROI. Figure 5A presents representative mid-transverse micro-CT images illustrating the trabecular bone microarchitecture in each group. Compared to the control group, the CKD group exhibited a significantly diminished BV/TV ratio and reduced trabecular number, with the observed differences reaching statistical significance (both p -values < 0.01). Moreover, statistically significant intergroup differences were detected in trabecular thickness and trabecular separation. Compared to the control group, the CKD group exhibited significantly decreased trabecular thickness and increased trabecular separation (all p -values = 0.03, Figure 5B). Thus, micro CT images are useful for showing CKD-induced changes in trabecular bone architecture.

3.5 | Histologic Analysis

In hematoxylin–eosin–stained sections, the abdominal aorta was normal in appearance in the control group and had a considerably reduced vascular luminal diameter in the CKD group relative to that in the control group. Concurrently, vessel wall thickness was increased in the CKD group but remained normal in the control group (Figure 6A). Microscopic examination of vertebral bone marrow specimens revealed pronounced sinusoidal dilatation and extensive plasma retention as histological hallmarks in the CKD group (Figure 6B). Moreover, the adipocytes within the bone marrow exhibited conspicuous morphological alterations, appearing markedly irregular in shape and reduced in numerical density compared to the control group (Figure 6C). Quantitative analyses revealed significant reductions in adipocyte number and bone trabecular microarchitecture (p < 0.05),

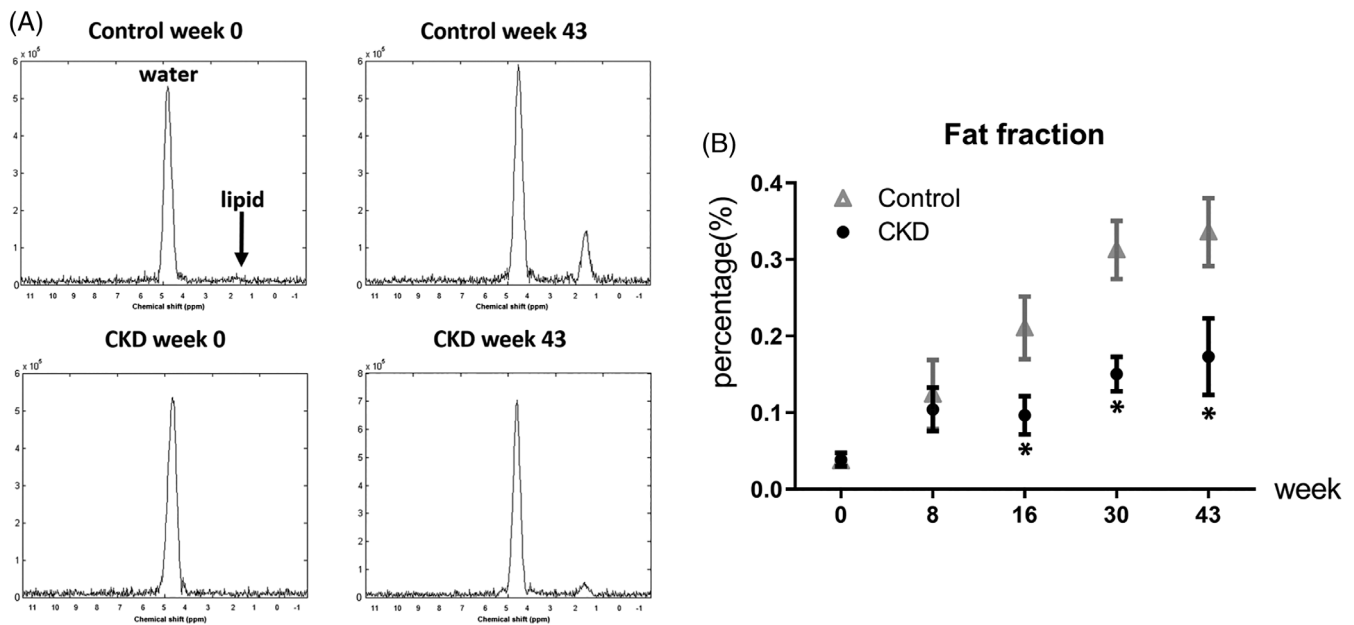


FIGURE 4 | Spectra and temporal changes in vertebral bone marrow fat fraction (FF) in the control and CKD groups. (A) Representative MRS illustrating water and lipid (arrow) spectra. At baseline (Week 0), a prominent water peak was observed at 4.7 ppm, while the lipid spectral peak at 1.33 ppm was absent in both the control and CKD groups (left column). At Week 43, the water spectral peak persisted in both groups, but a significantly lower lipid peak was observed in the CKD group (right column). (B) Longitudinal MRS study revealed that both groups showed significant increases in FF from baseline (Week 0) to Week 43. However, the CKD group exhibited lower FF compared to controls, with significant differences emerging from Week 16 onward ($p < 0.001$).

TABLE 5 | Longitudinal comparison of MRS FF values between the control and CKD groups using GEE analysis over a 43-week period.

	Parameters	<i>B</i>	Std. error	95% Wald CI		<i>p</i>
MRS FF values	Intercept	0.037	0.0019	0.033	0.041	< 0.001
	CKD vs. control	0.002	0.0038	-0.006	0.009	0.679
Evaluate temporal deviations from Week 0 in the control group	[Week = 43] vs. [Week = 0]	0.299	0.0164	0.267	0.331	< 0.001
	[Week = 30] vs. [Week = 0]	0.276	0.0137	0.249	0.302	< 0.001
	[Week = 16] vs. [Week = 0]	0.174	0.0152	0.144	0.204	< 0.001
	[Week = 8] vs. [Week = 0]	0.087	0.0171	0.053	0.120	< 0.001
Evaluate intergroup differences in temporal variations between the CKD and control groups	[Week = 43]	-0.164	0.0242	-0.211	-0.117	< 0.001
	[Week = 30]	-0.164	0.0173	-0.198	-0.130	< 0.001
	[Week = 16]	-0.116	0.0191	-0.153	-0.078	< 0.001
	[Week = 8]	-0.021	0.0208	-0.062	0.020	0.317

Note: *B*: regression coefficient, **p* value < 0.05.

accompanied by increased vessel density ($p = 0.003$), validating the MRI findings and indicating the occurrence of microstructural modifications (Figure 6D).

4 | Discussion

This study primarily investigated the alterations in blood perfusion and changes in the lumbar vertebral bone marrow microenvironment in rats after 5/6 nephrectomy, a model of CKD. Our results, to the best of our knowledge, are the first to demonstrate that 5/6 nephrectomy changes the DCE, T2*, and MRS values of vertebral bone marrow in animals and that these

changes correlate with histopathological results. Longitudinal MRI was employed to monitor changes in bone marrow vascularization, water, and fat content within the lumbar vertebrae. Complementary micro-CT and histological analyses were performed to validate the MRI findings and demonstrate the underlying associations. The results of this study could potentially provide valuable insights for non-invasively monitoring of the evolution and progression of spine osteodystrophy, a manifestation of mineral and bone disorders associated with CKD in human patients.

We employed DCE-MRI to quantify alterations in lumbar vertebral bone marrow perfusion over a prolonged period in the

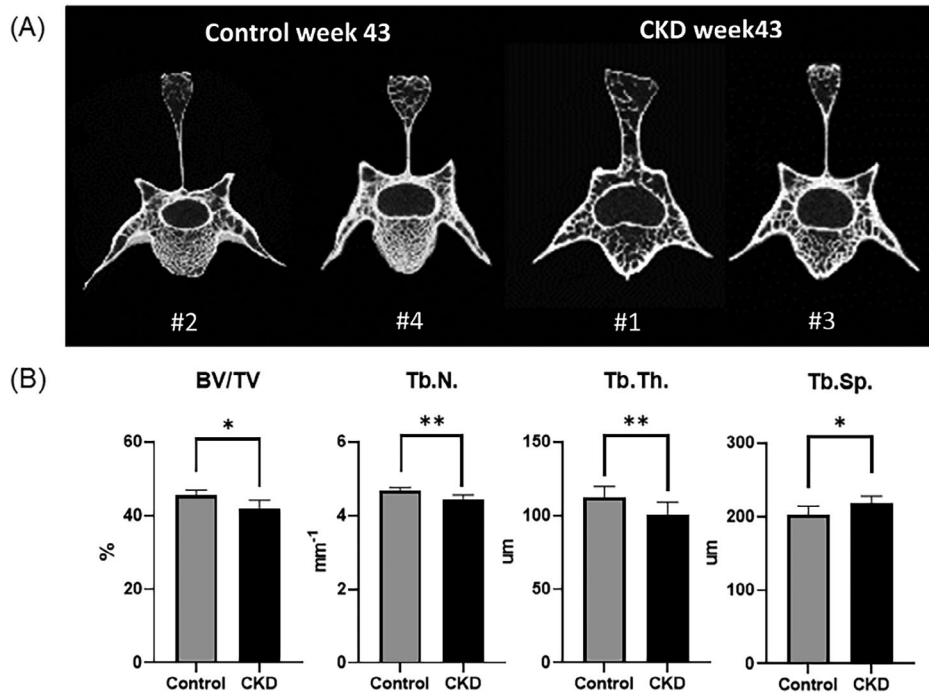


FIGURE 5 | Micro-CT analysis results of L5 vertebra. (A) Reconstructed micro-CT images revealed significant differences in bone microarchitecture between the CKD and control groups. The numbers below denote the case number of rats. Compact trabecular structure can be observed in control rats (Cases #2 and #4, left). Less trabeculation and increased separation were found in the CKD group (Cases #1 and #3, right). (B) Quantitative analysis of L5 vertebral bone marrow showed that the CKD group exhibited a diminished BV/TV ratio and reduced trabecular number ($p < 0.01$ for both parameters). Additionally, trabecular thickness was significantly decreased in the CKD group. Trabecular separation was significantly increased in the CKD group compared to controls ($p = 0.03$). BV/TV, bone volume/total volume; Tb.N., trabecular number; Tb.Th., trabecular thickness; Tb.Sp., trabecular separation.

CKD rat model relative to healthy controls. The microvascular architecture within the bone marrow milieu exhibits heightened vulnerability to the deleterious consequences of CKD, with potential manifestations including intimal hyperplasia and vascular lumen constriction, thereby compromising perfusion dynamics. From our assessment of the DCE-MRI results, A and k_{el} were significantly attenuated in the CKD group, suggesting reduced vertebral blood flow in CKD animals. The impaired renal function in CKD likely led to venous pressure changes, manifesting as decreased k_{el} and consequent augmentation of venous blood pooling within the dilated sinusoidal spaces. This venous outflow obstruction, compounded by the narrowed vascular lumina, may have progressively attenuated the trans-capillary solute exchange kinetics, as evidenced by the decline (though not significant decline) in the permeability-surface area product parameter k_{ep} (Figure 2C). The increased vessel density shown in Figure 6D represents a pathological vascular remodeling process characterized by sinus dilatation and vessel wall impairment, suggestive of an underlying compensatory mechanism in response to microvascular compromise. This phenomenon reflects a complex hypoperfusion state, where apparent vessel proliferation masks significant structural vascular dysfunction and reduced effective tissue perfusion. Notably, T2* quantitative imaging revealed elevated T2* values in the bone marrow of CKD animals, indicative of increased water content. Meanwhile, histological examination revealed sinusoidal dilatation and mild bone marrow edema as the underlying cause for the increased

T2* signal. A phenomenon akin to the T2* hyperintensities observed in hepatic sinusoidal dilatation has been associated with liver inflammation or fibrosis [38, 39]. We postulate that the elevated T2* values in the CKD group may be ascribed to increased plasma pooling within the dilated sinusoidal spaces and an increase in bone marrow water content.

Numerous prior studies have demonstrated that with aging, the hematopoietic red bone marrow gradually undergoes conversion to fatty yellow marrow, primarily composed of adipocytes [40, 41]. Additionally, research employing ovariectomized rat models to simulate postmenopausal conditions has utilized MRS to investigate postmenopausal changes. This research showed that the void spaces resulting from bone loss are subsequently filled by adipose tissue [32, 42]. Moreover, MRS analyses in human patients with CKD have revealed alterations in vertebral bone marrow fat content [43], further supporting the notion that adipocytes tend to occupy regions depleted of bone mass. Interestingly, our findings diverged from these previous observations, as we detected a relative decrease in vertebral bone marrow fat fraction (FF) in the CKD group compared to controls. We postulate that this discrepancy may be attributable to the metabolic disorders associated with CKD. In addition to compromising mineral metabolism, impaired renal clearance may cause the accumulation of uremic toxins in the bloodstream [44–46], and hyperuricemia has been implicated in modulating the differentiation capacity of mesenchymal stem cells (MSCs) [47]. MSCs in the bone marrow niche are

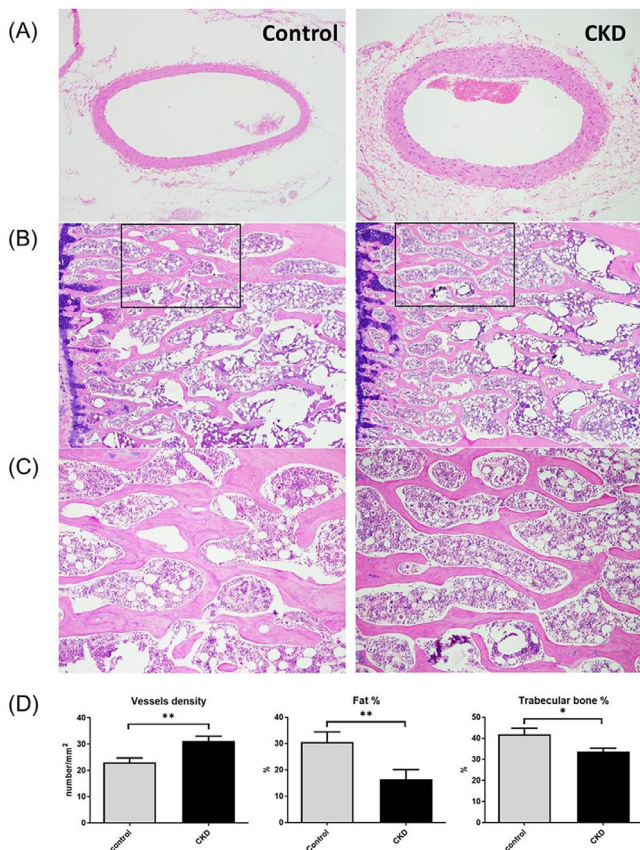


FIGURE 6 | Histopathological staining of the abdominal aorta and vertebral bone marrow in the control and CKD groups at Week 43. (A) H&E staining revealed reduced luminal diameter and increased vessel wall thickness in the CKD group. (B) Representative stains of vertebral bone marrow showed prominent sinusoidal dilatation and extensive plasma retention in the CKD group. (C) Magnified images show decreased numerical density of adipocytes and reduced trabecular number in CKD bone marrow relative to control rats. (D) Quantitative analyses revealed statistically significant reductions in adipocyte number (middle) and bone trabecular microarchitecture (right), accompanied by significant increases in vessel density (left), indicative of substantive microstructural modifications. [(A) and (C) $\times 100$, (B) $\times 40$ magnification.]

progenitors for osteoblasts and adipocytes. In youth, MSCs tend toward osteoblastic differentiation; with aging, they shift toward adipogenic differentiation, underlying the age-related transition from red to yellow marrow [40]. Elevated uric acid levels can suppress adipogenic differentiation, potentially explaining the decreased bone marrow fat content observed in our CKD group via MRS. [48] However, our study could not determine whether uric acid modulates MSC lineage commitment or directly impedes adipogenic differentiation. The 43-week observational period may have limited our ability to evaluate late-stage disease manifestations, and species-specific differences could explain discrepancies with human studies. μ CT investigations revealed reduced bone volume, trabecular number, and thickness, with increased trabecular separation in the vertebral bodies of CKD animals, evidencing CKD's detrimental effects on skeletal integrity. These findings align with previous research showing CKD-facilitated bone

loss, primarily due to dysregulated mineral metabolism and consequent FGF-23 secretion by bone cells [49].

The possible pathophysiology of bone degeneration encompasses a complex cascade of molecular mechanisms involving vascular dysfunction, marrow deterioration, and trabecular bone loss [50, 51]. Vascular compromise originates from endothelial dysfunction, characterized by reduced nitric oxide production and elevated endothelin-1 expression, alongside impaired angiogenesis through VEGF signaling disruption and inflammatory-mediated microvascular alterations [52, 53]. Concurrent bone marrow deterioration manifests through elevated oxidative stress, cellular senescence activation via p16INK4a/Rb and p53/p21 pathways, and stem cell niche disruption through CXCL12/CXCR4 axis dysregulation [54, 55]. These changes are accompanied by trabecular bone degradation, driven by disrupted RANKL/RANK signaling and Wnt/ β -catenin pathway perturbations, coupled with compromised osteoblast function and accelerated matrix degradation [56, 57]. This interconnected degradation cascade creates a self-perpetuating cycle where vascular insufficiency induces hypoxia, promoting inflammation and oxidative stress, thereby exacerbating both marrow and trabecular bone deterioration [58–60].

Our study has several limitations. The study exclusively utilized male rats as experimental subjects. This single-gender approach was adopted to simplify the animal model and reduced potential confounding factors associated with the hormonal fluctuations inherent to phases of the female reproductive cycle, such as menopause. Furthermore, in adherence to the ethical principles of the 3Rs governing animal research, the study design aimed to minimize unnecessary animal sacrifice and reduce overall animal usage. Consequently, a sham surgical procedure was not performed on the control group. This decision was supported by previous studies showing the minimal effects of sham surgery and attributing the observed changes to CKD rather than surgical trauma or other extraneous factors [61–64]. Moreover, the current study design could not clarify the potential impact of intact parathyroid gland function on the observed outcomes. Future investigations specifically aimed at delineating the interplay between parathyroid hormone homeostasis and the observed vertebral bone marrow alterations would be warranted to comprehensively elucidate the underlying pathophysiological mechanisms. Lastly, the histological analyses did not involve quantitative assessments of specific biomarkers.

In conclusion, this longitudinal multimodal MRI study used a 5/6 nephrectomy rat model to investigate the adverse effects of CKD on vertebral bone marrow perfusion dynamics, degenerative status, and adiposity. DCE-MRI, T2* mapping, MRS, and μ CT revealed CKD-induced impairments in skeletal blood supply, consequently disrupting bone marrow perfusion kinetics, altering marrow composition, and causing trabecular bone loss. Notably, vertebral bone marrow adiposity was markedly reduced in CKD animals compared to healthy controls, providing insights into the intrinsic pathophysiological cascades underlying the skeletal manifestations of CKD. The multiparametric imaging strategies employed in this study could enhance the effectiveness of monitoring techniques and therapeutic interventions by clarifying the pathophysiological

mechanisms underlying CKD. Moreover, these quantitative MRI techniques combined with μ CT hold promise as reliable methods for longitudinally tracking the progression of CKD-related bone marrow disease and associated skeletal complications. Based on these comprehensive imaging findings, we propose an integrated therapeutic strategy that addresses the challenge posed by the observed vascular dysfunction and skeletal deterioration. Our approach emphasizes early intervention through cardiovascular optimization and angiogenic therapies, coupled with bone-specific treatments to preserve trabecular architecture. Implementation of this strategy necessitates a multidisciplinary care model combining cardiovascular, nephrological, and orthopedic expertise. This personalized treatment approach, guided by advanced imaging monitoring, offers a promising pathway for improved management of CKD-related bone disorders.

Author Contributions

Guo-Shu Huang, Shih-Wei Chiang, and Chao-Ying Wang contributed to the study concept and design, procurement of study funds, performance of experiments, and data analysis and interpretation; Yi-Jen Peng, Skye Hsin-Hsien Yeh, and Yu-Juei Hsu provided study materials, performed experiments, and conducted data analysis and interpretation; Yu-Ching Chou, Heng-Han Chang, and Heng-Sheng Lee contributed to data analysis and interpretation, as well as statistical analysis; Ying-Chun Liu collected and assembled the data. All authors contributed to writing the manuscript, read and approved the submitted version, and revised the manuscript.

Acknowledgments

The authors would like to show gratitude to Dennis W Hwang and Ming-Huang Lin from the Institute of Biomedical Sciences, Academic Sinica, whose insight, expertise, and technical knowledge greatly assisted in carrying out this research. The study was supported by grants from the National Science and Technology Council of Taiwan (MOST102-2628-B-016-004-MY3 and MOST 108-2314-B-016-007-MY2) and the Civilian Foundation of Tri-Service General Hospital (TSGH-C103-051 and TSGH-C104-048).

Conflicts of Interest

The authors declare no conflicts of interest.

References

1. K. Matsushita, S. H. Ballew, A. Y. Wang, R. Kalyesubula, E. Schaeffner, and R. Agarwal, "Epidemiology and Risk of Cardiovascular Disease in Populations With Chronic Kidney Disease," *Nature Reviews Nephrology* 18, no. 11 (2022): 696–707.
2. Q. Luo, X. Xia, B. Li, Z. Lin, X. Yu, and F. Huang, "Serum Uric Acid and Cardiovascular Mortality in Chronic Kidney Disease: A Meta-Analysis," *BMC Nephrology* 20, no. 1 (2019): 18.
3. D. H. Kofod, N. Carlson, E. F. Ballegaard, et al., "Cardiovascular Mortality in Patients With Advanced Chronic Kidney Disease With and Without Diabetes: A Nationwide Cohort Study," *Cardiovascular Diabetology* 22, no. 1 (2023): 140.
4. P. Evenepoel, B. Opdebeeck, K. David, and P. C. D'Haese, "Bone-Vascular Axis in Chronic Kidney Disease," *Advances in Chronic Kidney Disease* 26, no. 6 (2019): 472–483.
5. P. D. Miller, "Chronic Kidney Disease and the Skeleton," *Bone Research* 2 (2014): 14044.

6. C. Vachey, A. Candellier, S. Toutain, and F. Mac-Way, "The Bone-Vascular Axis in Chronic Kidney Disease: From Pathophysiology to Treatment," *Current Osteoporosis Reports* 22, no. 1 (2024): 69–79.
7. E. Neven and P. C. D'Haese, "Vascular Calcification in Chronic Renal Failure: What Have We Learned From Animal Studies?," *Circulation Research* 108, no. 2 (2011): 249–264.
8. C. M. Shanahan, M. H. Crouthamel, A. Kapustin, and C. M. Giachelli, "Arterial Calcification in Chronic Kidney Disease: Key Roles for Calcium and Phosphate," *Circulation Research* 109, no. 6 (2011): 697–711.
9. H. Komaba and M. Fukagawa, "FGF23: A Key Player in Mineral and Bone Disorder in CKD," *Nefrologia* 29, no. 5 (2009): 392–396.
10. L. Kalichman and D. J. Hunter, "Diagnosis and Conservative Management of Degenerative Lumbar Spondylolisthesis," *European Spine Journal* 17, no. 3 (2008): 327–335.
11. K. M. Cheung, J. Karppinen, D. Chan, et al., "Prevalence and Pattern of Lumbar Magnetic Resonance Imaging Changes in a Population Study of One Thousand Forty-Three Individuals," *Spine* 34, no. 9 (2009): 934–940.
12. G. S. Travlos, "Normal Structure, Function, and Histology of the Bone Marrow," *Toxicologic Pathology* 34, no. 5 (2006): 548–565.
13. V. W. Yu and D. T. Scadden, "Heterogeneity of the Bone Marrow Niche," *Current Opinion in Hematology* 23, no. 4 (2016): 331–338.
14. S. P. Sourbron and D. L. Buckley, "Tracer Kinetic Modelling in MRI: Estimating Perfusion and Capillary Permeability," *Physics in Medicine and Biology* 57, no. 2 (2012): R1–R33.
15. M. D. Sweeney, A. P. Sagare, and B. V. Zlokovic, "Blood-Brain Barrier Breakdown in Alzheimer Disease and Other Neurodegenerative Disorders," *Nature Reviews Neurology* 14, no. 3 (2018): 133–150.
16. H. Nilsson, L. Blomqvist, L. Douglas, et al., "Gd-EOB-DTPA-Enhanced MRI for the Assessment of Liver Function and Volume in Liver Cirrhosis," *British Journal of Radiology* 86, no. 1026 (2013): 20120653.
17. A. Kido, K. Fujimoto, T. Okada, and K. Togashi, "Advanced MRI in Malignant Neoplasms of the Uterus," *Journal of Magnetic Resonance Imaging* 37, no. 2 (2013): 249–264.
18. E. Furman-Haran, M. S. Feinberg, D. Badikhi, E. Eyal, T. Zehavi, and H. Degani, "Standardization of Radiological Evaluation of Dynamic Contrast Enhanced MRI: Application in Breast Cancer Diagnosis," *Technology in Cancer Research & Treatment* 13, no. 5 (2014): 445–454.
19. H. J. Bining, R. Santos, G. Andrews, and B. B. Forster, "Can T2 Relaxation Values and Color Maps Be Used to Detect Chondral Damage Utilizing Subchondral Bone Marrow Edema as a Marker?," *Skeletal Radiology* 38, no. 5 (2009): 459–465.
20. M. A. Brinckman, C. Chau, and J. S. Ross, "Marrow Edema Variability in Acute Spine Fractures," *Spine Journal* 15, no. 3 (2015): 454–460.
21. G. P. Liney, C. P. Bernard, D. J. Manton, L. W. Turnbull, and C. M. Langton, "Age, Gender, and Skeletal Variation in Bone Marrow Composition: A Preliminary Study at 3.0 Tesla," *Journal of Magnetic Resonance Imaging* 26, no. 3 (2007): 787–793.
22. C. Grunfeld, M. Saag, J. Cofrancesco, Jr., et al., "Study of Fat Redistribution and Metabolic Change in HIV Infection (FRAM). Regional Adipose Tissue Measured by MRI Over 5 Years in HIV-Infected and Control Participants Indicates Persistence of HIV-Associated Lipodystrophy," *AIDS* 24, no. 11 (2010): 1717–1726.
23. D. Schellinger, C. S. Lin, H. G. Hatipoglu, and D. Fertikh, "Potential Value of Vertebral Proton MR Spectroscopy in Determining Bone Weakness," *American Journal of Neuroradiology* 22, no. 8 (2001): 1620–1627.
24. C. Borelli, D. Vergara, R. Guglielmi, F. Aucella, V. Testini, and G. Guglielmi, "Assessment of Bone Marrow Fat by 3-Tesla Magnetic Resonance Spectroscopy in Patients With Chronic Kidney Disease,"

- Quantitative Imaging in Medicine and Surgery* 13, no. 11 (2023): 7432–7443.
25. C. Y. Lin, Y. J. Hsu, S. C. Hsu, et al., “CB1 Cannabinoid Receptor Antagonist Attenuates Left Ventricular Hypertrophy and Akt-Mediated Cardiac Fibrosis in Experimental Uremia,” *Journal of Molecular and Cellular Cardiology* 85 (2015): 249–261.
26. G. Brix, W. Semmler, R. Port, L. R. Schad, G. Layer, and W. J. Lorenz, “Pharmacokinetic Parameters in CNS Gd-DTPA Enhanced MR Imaging,” *Journal of Computer Assisted Tomography* 15, no. 4 (1991): 621–628.
27. K. V. Lund, T. G. Simonsen, G. B. Kristensen, and E. K. Rofstad, “Pharmacokinetic Analysis of DCE-MRI Data of Locally Advanced Cervical Carcinoma With the Brix Model,” *Acta Oncologica* 58, no. 6 (2019): 828–837.
28. H. T. Ma, J. F. Griffith, D. K. Yeung, and P. C. Leung, “Modified Brix Model Analysis of Bone Perfusion in Subjects of Varying Bone Mineral Density,” *Journal of Magnetic Resonance Imaging* 31, no. 5 (2010): 1169–1175.
29. C. Wang, X. Zhang, X. Liu, et al., “Improved Liver R2* Mapping by Pixel-Wise Curve Fitting With Adaptive Neighborhood Regularization,” *Magnetic Resonance in Medicine* 80, no. 2 (2018): 792–801.
30. M. Salas-Ramirez, J. Tran-Gia, C. Kesenheimer, et al., “Quantification of Fat Fraction in Lumbar Vertebrae: Correlation With Age and Implications for Bone Marrow Dosimetry in Molecular Radiotherapy,” *Physics in Medicine and Biology* 63, no. 2 (2018): 025029.
31. B. Mengiardi, M. R. Schmid, N. Boos, et al., “Fat Content of Lumbar Paraspinal Muscles in Patients With Chronic Low Back Pain and in Asymptomatic Volunteers: Quantification With MR Spectroscopy,” *Radiology* 240, no. 3 (2006): 786–792.
32. G. W. Li, G. Y. Tang, Y. Liu, R. B. Tang, Y. F. Peng, and W. Li, “MR Spectroscopy and Micro-CT in Evaluation of Osteoporosis Model in Rabbits: Comparison With Histopathology,” *European Radiology* 22, no. 4 (2012): 923–929.
33. H. K. Genant, K. Engelke, and S. Prevrhal, “Advanced CT Bone Imaging in Osteoporosis,” *Rheumatology* 47, no. Suppl 4 (2008): 9–16.
34. Y. Tada and T. Sato, “A Bias-Reduced Generalized Estimating Equation Approach for Proportional Odds Models With Small-Sample Longitudinal Ordinal Data,” *BMC Medical Research Methodology* 24, no. 1 (2024): 140.
35. S. L. Zeger, K. Y. Liang, and P. S. Albert, “Models for Longitudinal Data: A Generalized Estimating Equation Approach,” *Biometrics* 44, no. 4 (1988): 1049–1060.
36. P. E. Shrout and J. L. Fleiss, “Intraclass Correlations: Uses in Assessing Rater Reliability,” *Psychological Bulletin* 86, no. 2 (1979): 420–428.
37. T. K. Koo and M. Y. Li, “A Guideline of Selecting and Reporting Intraclass Correlation Coefficients for Reliability Research,” *Journal of Chiropractic Medicine* 15, no. 2 (2016): 155–163.
38. G. Brancatelli, A. Furlan, A. Calandra, and B. M. Dioguardi, “Hepatic Sinusoidal Dilatation,” *Abdominal Radiology* 43, no. 8 (2018): 2011–2022.
39. H. Laumonier, P. Bioulac-Sage, C. Laurent, J. Zucman-Rossi, C. Balabaud, and H. Trillaud, “Hepatocellular Adenomas: Magnetic Resonance Imaging Features as a Function of Molecular Pathological Classification,” *Hepatology* 48, no. 3 (2008): 808–818.
40. B. J. Bain, “Bone Marrow Aspiration,” *Journal of Clinical Pathology* 54, no. 9 (2001): 657–663.
41. A. G. Veldhuis-Vlug and C. J. Rosen, “Mechanisms of Marrow Adiposity and Its Implications for Skeletal Health,” *Metabolism* 67 (2017): 106–114.
42. J. Zhu, L. Zhang, X. Wu, et al., “Reduction of Longitudinal Vertebral Blood Perfusion and Its Likely Causes: A Quantitative Dynamic Contrast-Enhanced MR Imaging Study of a Rat Osteoporosis Model,” *Radiology* 282, no. 2 (2017): 369–380.
43. R. N. Moorthi, W. Fadel, G. J. Eckert, K. Ponsler-Sipes, S. M. Moe, and C. Lin, “Bone Marrow Fat Is Increased in Chronic Kidney Disease by Magnetic Resonance Spectroscopy,” *Osteoporosis International* 26, no. 6 (2015): 1801–1807.
44. D. I. Jalal, M. Chonchol, W. Chen, and G. Targher, “Uric Acid as a Target of Therapy in CKD,” *American Journal of Kidney Diseases* 61, no. 1 (2013): 134–146.
45. R. J. Johnson, T. Nakagawa, D. Jalal, L. G. Sánchez-Lozada, D. H. Kang, and E. Ritz, “Uric Acid and Chronic Kidney Disease: Which Is Chasing Which?,” *Nephrology, Dialysis, Transplantation* 28, no. 9 (2013): 2221–2228.
46. Y. P. Siu, K. T. Leung, M. K. Tong, and T. H. Kwan, “Use of Allopurinol in Slowing the Progression of Renal Disease Through Its Ability to Lower Serum Uric Acid Level,” *American Journal of Kidney Diseases* 47, no. 1 (2006): 51–59.
47. P. L. Riches, A. F. Wright, and S. H. Ralston, “Recent Insights Into the Pathogenesis of Hyperuricaemia and Gout,” *Human Molecular Genetics* 18, no. 2 (2009): 177–184.
48. H. Z. Li, Z. Chen, C. L. Hou, Y. X. Tang, F. Wang, and Q. G. Fu, “Uric Acid Promotes Osteogenic Differentiation and Inhibits Adipogenic Differentiation of Human Bone Mesenchymal Stem Cells,” *Journal of Biochemical and Molecular Toxicology* 29, no. 8 (2015): 382–387.
49. S. Fukumoto and Y. Shimizu, “Fibroblast Growth Factor 23 as a Phosphotropic Hormone and Beyond,” *Journal of Bone and Mineral Metabolism* 29, no. 5 (2011): 507–514.
50. S. K. Ramasamy, A. P. Kusumbe, L. Wang, and R. H. Adams, “Endothelial Notch Activity Promotes Angiogenesis and Osteogenesis in Bone,” *Nature* 507, no. 7492 (2014): 376–380.
51. A. P. Kusumbe, S. K. Ramasamy, T. Itkin, et al., “Age-Dependent Modulation of Vascular Niches for Haematopoietic Stem Cells,” *Nature* 532, no. 7599 (2016): 380–384.
52. R. J. van’t Hof and S. H. Ralston, “Nitric Oxide and Bone,” *Immunology* 103, no. 3 (2001): 255–261.
53. C. Maes, T. Kobayashi, M. K. Selig, et al., “Osteoblast Precursors, but Not Mature Osteoblasts, Move Into Developing and Fractured Bones Along With Invading Blood Vessels,” *Developmental Cell* 19, no. 2 (2010): 329–344.
54. C. Hellmich, E. Wojtowicz, J. A. Moore, et al., “p16INK4A-Dependent Senescence in the Bone Marrow Niche Drives Age-Related Metabolic Changes of Hematopoietic Progenitors,” *Blood Advances* 7, no. 2 (2023): 256–268.
55. S. Scala, “Molecular Pathways: Targeting the CXCR4-CXCL12 Axis—Untapped Potential in the Tumor Microenvironment,” *Clinical Cancer Research* 21, no. 19 (2015): 4278–4285.
56. B. F. Boyce and L. Xing, “Functions of RANKL/RANK/OPG in Bone Modeling and Remodeling,” *Archives of Biochemistry and Biophysics* 473, no. 2 (2008): 139–146.
57. F. Marini, F. Giusti, G. Palmi, and M. L. Brandi, “Role of Wnt Signaling and Sclerostin in Bone and as Therapeutic Targets in Skeletal Disorders,” *Osteoporosis International* 34, no. 2 (2023): 213–238.
58. P. Ramalingam, J. M. Butler, and M. G. Poulos, “Vascular Regulation of Hematopoietic Stem Cell Homeostasis, Regeneration, and Aging,” *Current Stem Cell Reports* 7, no. 4 (2021): 194–203.
59. P. Eliasson and J. I. Jönsson, “The Hematopoietic Stem Cell Niche: Low in Oxygen but a Nice Place to Be,” *Journal of Cellular Physiology* 222, no. 1 (2010): 17–22.
60. S. Méndez-Ferrer, T. V. Michurina, F. Ferraro, et al., “Mesenchymal and Haematopoietic Stem Cells Form a Unique Bone Marrow Niche,” *Nature* 466, no. 7308 (2010): 829–834.

61. D. H. Kang, A. H. Joly, S. W. Oh, et al., "Impaired Angiogenesis in the Remnant Kidney Model: I. Potential Role of Vascular Endothelial Growth Factor and Thrombospondin-1," *Journal of the American Society of Nephrology* 12, no. 7 (2001): 1434–1447.
62. K. A. Griffin, M. Picken, and A. K. Bidani, "Method of Renal Mass Reduction Is a Critical Modulator of Subsequent Hypertension and Glomerular Injury," *Journal of the American Society of Nephrology* 4, no. 12 (1994): 2023–2031.
63. Z. Lu, Y. Xie, X. Liu, et al., "Effect of 5/6 Nephrectomized Rat Serum on Epithelial-To-Mesenchymal Transition In Vitro," *Renal Failure* 33, no. 6 (2011): 600–608.
64. A. L. Gava, F. P. Freitas, C. M. Balarini, E. C. Vasquez, and S. S. Meyrelles, "Effects of 5/6 Nephrectomy on Renal Function and Blood Pressure in Mice," *International Journal of Physiology, Pathophysiology and Pharmacology* 4, no. 3 (2012): 167–173.